Spin-forbidden and spin-enabled $4f^{14} \rightarrow 4f^{13}5d^1$ transitions of Yb^{2+}-doped $CsCaBr_3$.

Goar Sánchez-Sanz,[1] Luis Seijo,[1,2] and Zoila Barandiarán[1,2,*]

[1]*Departamento de Química, C-XIV,*
Universidad Autónoma de Madrid, 28049 Madrid, Spain
[2]*Instituto Universitario de Ciencia de Materiales Nicolás Cabrera,*
Universidad Autónoma de Madrid, 28049 Madrid, Spain

(Dated: April 24, 2009)

Abstract

The lowest part of the $4f \rightarrow 5d$ absorption spectrum of Yb^{2+}-doped $CsCaBr_3$ crystals has been calculated using methods of quantum chemistry and it is presented here. A first, low-intensity band is found on the low energy side of the spectrum, followed by several strong absorption bands, in agreement with experimental observations in trivalent and divalent lanthanide ions of the second half of the lanthanide series, doped in crystals. Based on Hund's rule, these transitions are usually interpreted as "spin-forbidden" and "spin-allowed" transitions, but this interpretation has been recently questioned in the literature. Here, a two-step relativistic method has been used which reveals the spin composition of the excited state wave functions. The forbidden band is found to be due to "spin-forbidden" transitions involving "high-spin" excited states because their 1^3T_{1u} character is 90%. However, the allowed bands cannot be described as "spin-allowed" transitions involving "low-spin" excited states. Rather, they correspond to "spin-enabled" transitions because they get their intensity from limited (smaller than 45%) electric dipole enabling low-spin $^1T_{1u}$ character. Calculations using a spin-free Hamiltonian revealed that the difference in their electronic structures is related to the fact that the $4f^{13}5d(t_{2g})^1$ manifold is split by an energy gap which separates the lowest (high-spin) 1^3T_{1u} from the rest of terms, which, in turn, lie very close in energy from each other. As a consequence, the lowest spin-orbit components of 1^3T_{1u} are shown to remain 90% pure when spin-orbit coupling is considered, whereas a strong spin-orbit coupling exists between the remaining $4f^{13}5d(t_{2g})^1$ terms, among which the 1–3 $^1T_{1u}$ enabling ones lie. As a result, there is a widespread electric dipole enabling $^1T_{1u}$ character, which, although never higher than 45%, leads to a number of spin-enabled absorption bands.

I. INTRODUCTION

The interest of spectroscopic studies of lanthanide ions in solids has constantly increased motivated by their widening field of applications and favored by the rapidly growing capability of the experimental techniques. This has resulted in significant progress in the understanding of their electronic structure, particularly, the $4f^N$ manifolds of trivalent lanthanides (Ln^{3+}), which, in turn, has led the scientific community to face new challenges posed by higher energy levels and less stable oxidation states. An increased effort has been done recently in the study of the $4f^{N-1}5d^1$ states of Ln^{3+}, in spite of the fact that they occur at very high energies, in the UV-VUV spectral range. Representative of these works are the systematic study of the $4f^N \rightarrow 4f^{N-1}5d^1$ transitions of the light ($N \leq 7$) (Ref. 1) and heavy ($N > 7$) (Ref. 2) lanthanides in various wide band gap hosts and the works referenced therein. This effort has influenced and renewed the interest on the $4f^{N-1}5d^1$ states of the isoelectronic series of divalent lanthanide ions (Ln^{2+}), since, even though the divalent oxidation state is more difficult to stabilize in solid matrices, their $4f^N \rightarrow 4f^{N-1}5d^1$ excitations occur at much lower energies, in the near-IR, visible, and near-UV. An overview of Ln^{2+} works can be found in Ref. 3.

A basic finding, emerging from the comparison between high resolution $4f^N \rightarrow 4f^{N-1}5d^1$ excitation spectra of light and heavy Ln^{3+}, is the occurrence of low-intensity bands on the low energy side of the spectra of the $N > 7$ members followed by several strong $4f^N \rightarrow 4f^{N-1}5d^1$ bands.[1,2] Invoking Hund's rule the weak bands have been associated with transitions from the $4f^N$ ($N > 7$) ground state to high-spin $4f^{N-1}5d^1$ states whereas the strong bands have been interpreted as transitions to low-spin $4f^{N-1}5d^1$ states,[4,5] and, for this reason, they have been called spin-forbidden and spin-allowed bands, respectively.[5] The energy separation between the lowest spin-forbidden and lowest spin-allowed transitions has also been investigated across the series and it has been found to decrease from Tb^{3+} ($\sim$8000 cm^{-1}) to Tm^{3+} ($\sim$2000 cm^{-1}).[2,6] Spin-forbidden and spin-allowed emission bands have also been observed in Er^{3+} and Tm^{3+} in fluorides with decay times in the μs and ns scales, respectively, which is consistent with their forbidden and allowed nature.[5]

Similar spectral features, namely, weak bands followed by strong bands at higher energies, have been found in heavy Ln^{2+} ions in solids, particularly in Tm^{2+} (Refs. 7–11) and Yb^{2+} (Refs. 3,10), where the $4f^{N-1}5d^1$ manifold is well separated from the $4f^N$ states, but also in

Dy^{2+} doped in $KMgF_3$.[10] In analogy with the previous works on Ln^{3+} referred above,[2,5] they have been interpreted as spin-forbidden and spin-allowed transitions, respectively.[7,8,10,11]

However, a recent work on Yb^{2+}-doped $SrCl_2$ (Ref. 3) has challenged these interpretations by concluding that the distinction of the states involved is rather based on orbital symmetry than on spin composition, since all of the lower $4f^{N-1}5d^1$ states are predominantly high-spin. Furthermore, the authors stress that the energy separation between high-spin and low-spin states cannot be inferred by inspection of spectral data but requires calculation, because most $4f^{N-1}5d^1$ states are of mixed spin parentage. These conclusions have been drawn from crystal field calculations and analyses.[3]

In these circumstances, the point of view of quantum chemistry on what is the high-spin and low-spin character of the lowest $4f^{N-1}5d^1$ states of heavy divalent lanthanide ions in solids and how does this character molds their spectral features is useful, and it is the main goal of this work.

For this purpose, *ab initio* relativistic methods of quantum chemistry like the one we use here, which proceed in two-steps, are particularly useful: In a first step, a scalar relativistic (spin-orbit free) Hamiltonian is used and the focus is on a proper description of electron correlation, for which sate-of-the-art wave function based methods are used. At this stage, spin is a good quantum number and the energy differences between high- and low-spin states are well defined. In a second step, the effects of electron correlation are transferred to a spin dependent Hamiltonian and spin-orbit (SO) configuration interaction (CI) calculations are done in a relatively small, energy-shifted determinantal space. The resulting spin-orbit wave functions are expressed in terms of states of all possible spin multiplicities, so that their high-spin and low-spin character is traced back. Also, the resulting transition energies and spectral properties (including absorption and emission band shapes) can be related to the high- and low-spin character and to the high- and low-spin energy differences obtained in the first step.

Yb^{2+} is the most suited heavy divalent lanthanide ion for this study, because its $4f^{14}$ ground state is a pure spin singlet, a pure low-spin state, which focuses the theoretical analyses on the $4f^{13}5d^1$ excited states. It is known that Yb^{2+} can be stabilized in $CsCaBr_3$,[9] which is a very interesting host because it has been recently shown that it favors multiple emissions in heavy Ln^{2+} ions like Tm^{2+}.[7] Therefore, the $CsCaBr_3$:Yb^{2+} crystal is a good choice for the basic research intended here. Moreover, the study of the electronic structure

of even higher excited states, addressed in a separate work,[12] should reveal its potentiality as a multiply luminescent material. Altogether, the analyses and predictions of quantum chemistry in this material result in a deeper understanding of the lowest part of the spectrum (also applicable to other heavy lanthanides, as discussed) and serve to evaluate possible luminescent properties which could make future experimental work worth the effort.

Consequently, we have calculated the lowest $4f^{14}\rightarrow 4f^{13}5d^1$ absorption bands of $CsCaBr_3$:Yb^{2+} by means of *ab initio* methods of quantum chemistry applied to the octahedral $(YbBr_6)^{4-}$ defect cluster embedded in a reliable representation of $CsCaBr_3$. A first, low intensity band is found on the low energy side of the spectrum followed by several strong absorption bands, in agreement with the observations mentioned above. The electronic structure of the states leading to these two types of excitations appears to be very different: whereas the forbidden band can be described, according to the quantum chemical calculations and analyses, as "spin-forbidden" transitions involving "high-spin" excited states, the next allowed band (and all other allowed bands observed) can be described as "spin-enabled" transitions to excited states with strong spin-orbit mixing, which can neither be described as high-spin states nor as low-spin states, and which get their intensity from quite limited (smaller than 45%) low-spin $^1T_{1u}$ enabling character. This very different electronic structure is related to the fact that the lowest $4f^{13}5d(t_{2g})^1$ 1^3T_{1u} state is isolated from the rest of close-lying terms by an energy gap, which allows its lowest spin-orbit components to keep 90% of its high-spin character, whereas the transition enabling $^1T_{1u}$ states lie close in energy to other terms, this resulting in extensive spin-orbit mixing and a number of spin-enabled absorption bands. In turn, the energy separation of the lowest lying 1^3T_{1u} state is related to the energy separation of the lowest lying Yb^{2+} free ion $4f^{13}5d^1$–^3P term as calculated without spin-orbit interaction.[12] The details of the calculations are given in Section II; their results are discussed in Section III, and the conclusions appear in Section IV.

II. DETAILS OF THE CALCULATIONS

A number of applications on lanthanide[13,14] and actinide[15,16] ions in solids have revealed the adequacy of the relativistic *ab initio* model potential (AIMP) embedded cluster method,[17,18] in combination with correlation methods based on multireference wave functions,[19–23] as an acceptable methodological framework which allows for the calculation of the

local structure around an f-element impurity and its so-called f–f and f–d transitions in ionic crystals. Acceptable compromises between feasibility of the calculations and accuracy of the results have allowed to set reasonable standard choices for cluster size, molecular basis sets needed for the molecular orbital expansions, and active spaces that define the multiconfigurational set upon which correlated wave functions are built. We use here such standards specifying only the technical details. We refer to the methodological references for the details of the methods.

The standard choice for the defect cluster is to define it as the impurity plus its first neighbors: $(YbBr_6)^{4-}$, in this case, where Yb^{2+} ions substitute for Ca^{2+} ions at octahedral sites. The effects of the surrounding host ions are incorporated by the AIMP embedding potentials included in the cluster Hamiltonian. These potentials have been obtained in this work for the Cs^+, Ca^{2+}, and Br^- ions by performing self-consistent embedded ions calculations at the Hartree-Fock level, in the $CsCaBr_3$ perovskite using the experimental structure for cubic $CsCaBr_3$ (a_0 = 5.69 Å).[24] These total ion embedding AIMPs are used to represent the classical and quantum mechanical effects of the ions located within a cube of length $4a_0$ centered at the impurity site; point-charges are used for the remaining ions within a cube of length $7a_0$, using the nominal charges for all of them except the frontier ions, which bear fractional charges according to Evjen's method.[25]

Within the $(YbBr_6)^{4-}$ cluster, relativistic core AIMPs are used to represent the [Kr] core of Yb [26] and the [Ar, $3d$] cores of Br; [27] the corresponding Yb Gaussian valence basis set $(14s10p10d8f)$,[28] supplemented with three g-type functions that give maximum radial overlap with the $4f$ atomic orbital, was used contracted as $[6s5p6d4f1g]$. In the case of Br, the valence basis set used $(9s9p4d)[3s5p2d]$, includes three d-type orthogonality functions which give maximum radial overlap with the $3d$ core orbital, one d-type polarization function[29] and one p-type diffuse function for anions with orbital exponent $\zeta = 0.03681605$.[30] Basis functions have also been included at the second neighbor Ca sites to favor strong orthogonality with the environment; the Ca $(10s7p)$ set used in the preparatory self-consistent embedded ions calculations was used contracted as $[1s1p]$, which corresponds to the external Ca^{2+} $3s$ and $3p$ embedded atomic orbitals.

Electron correlation and spin-orbit coupling were combined together as follows: In a first, spin-orbit free step, state-average complete active space self consistent field calculations (SA-CASSCF)[19] were performed using the relativistic Wood-Boring AIMP[31] embedded

cluster Hamiltonian omitting the spin-orbit operators. These calculations account for embedding effects, scalar relativistic effects, and non-dynamic electron correlation within the $4f^{14}$, $4f^{13}5d^1$, and $4f^{13}6s^1$ manifolds of states. The active space results from distributing the 14 open-shell electrons in 13 active molecular orbitals with main character Yb $4f$, $5d$, $6s$, this being the standard choice of active space for a lanthanide; [32] it will be referred to as CASSCF($4f$,$5d$,$6s$). Dynamic electron correlation was taken into account using the SA-CASSCF wave functions in subsequent multistate second-order perturbation theory calculations (MS-CASPT2),[20–23] where 80 valence electrons occupying the cluster molecular orbitals with main character Br $4s$, $4p$ and Yb $4d$, $5s$, $5p$, $4f$, and $5d/6s$ were correlated; these calculations will be referred to as MS-CASPT2(Br48,Yb32). The program MOLCAS was used for these calculations.[33] In a second step of calculations with the full Wood-Boring AIMP Hamiltonian,[31] which includes the spin-orbit coupling operator (scaled by a factor of 0.9, as proposed in Ref. 34), we performed double-group spin-orbit configuration-interaction (CI) calculations. The shifting operator included in this Hamiltonian, the so-called spin-free-state-shifting ($sfss$) operator,[35] transports the dynamic electron correlation effects retrieved at the spin-orbit free MS-CASPT2(Br48,Yb32) level onto the smaller configurational space used in the spin-orbit CI calculations, which include the restricted active space formed by the $4f^{13}5d^1$ and $4f^{13}6s^1$ multireference plus all single excitations from the $4f$, $5d$, and $6s$ molecular orbitals to the virtual orbitals. For these calculations, the bases described above were truncated to Yb[$6s5p6d4f$], Br[$3s3p$]. We will refer to these calculations as SO-CI; they were done using the COLUMBUS package.[36] The EPCISO program[37] was used to calculate electric dipole transition moments. All AIMP data (for embedding and/or for cores) and valence basis sets can be found in Ref. 38.

The theoretical absorption profiles were produced using the SO-CI results and the semi-classical time-dependent approach of Heller[39–41] to calculate the a_{1g} vibrational envelope of each individual electric dipole allowed transition $4f^{14}$–1 $A_{1g} \rightarrow 4f^{13}5d(t_{2g})^1$– i T_{1u} (i = 1, 11). To do this, the calculated equilibrium distance and a_{1g} vibrational frequency of the ground and excited states were used together with the corresponding minimum-to-minimum energy differences and absorption oscillator strengths. The same procedures and methods were used in U^{4+}-doped Cs_2GeF_6; see Ref. 42 for details.

III. RESULTS AND DISCUSSION

As stated in the Introduction, the main objective of this work is to investigate the relationship between the spectral features of the lowest electronic $4f^N \rightarrow 4f^{N-1}5d^1$ transitions of heavy lanthanide ions in solids and the high- and low-spin character of the states involved applying *ab initio* methods of quantum chemistry to the representative system $CsCaBr_3$:Yb^{2+}. The lowest $4f^N \rightarrow 4f^{N-1}5d^1$ electronic transitions of the octahedral $(YbBr_6)^{4-}$ embedded cluster are found to have $4f^N \rightarrow 4f^{N-1}5d(t_{2g})^1$ main configurational character. Higher excited states are studied elsewhere.[12]

We report and discuss here the results following the two-step strategy of the relativistic quantum chemical calculations. In a first Subsection, the results of scalar relativistic (spin-orbit free) calculations are discussed, focusing on the effects of electron correlation and on the energy differences between high- and low-spin states (spin triplets and singlets, in our case). In a second Subsection, we discuss the results of spin-orbit calculations, the high- and low-spin character of the wave functions, and we relate the transition energies and spectral properties with the high- and low-spin character and with the high- and low-spin energy differences discussed in the first Subsection.

A. Spin-orbit free results: High-spin states, low-spin states, and their energy differences

The use of the AIMP embedding makes it possible to concentrate the methodological and computational effort on the $(YbBr_6)^{4-}$ embedded cluster electronic structure. For this fragment we have used state-of-the-art levels of methodology presently applicable to molecules containing heavy open-shell elements and having large manifolds of excited states (see Section II for details). Such high demands are related to two characteristics that are discussed and become apparent in this and the next Subsection, respectively. On the one hand, the impact of electron correlation in this system can be expected to be among the largest in the lanthanide series, both in terms of computational demands and in terms of transition energy corrections. On the other hand, relativistic effects including spin-orbit coupling, are crucial in a lanthanide bearing material, and the combination of this requirement with that of electron correlation, for so many excited states, suggests the convenience of the two-step

relativistic method used here.

The computational demands of electron correlation stem from the fact that the large number of open-shell electrons (14), distributed in the relevant valence molecular orbitals (with main character Yb $4f$, $5d$, and $6s$), produces a very large reference configurational space (the present SA-CASSCF calculations include some 10^5 configurations). Even so, this level of methodology is not able to represent the dynamic correlation effects properly, as it can be observed in Table I, where all high- ($^3\Gamma$) and low-spin ($^1\Gamma$) states of the $4f^{13}5d(t_{2g})^1$ manifold are shown and are found to be very close in energy to the ground state. Rather, the CASSCF wave functions are the basis on which dynamic correlation is treated pre-turbationally (MS-CASPT2 calculations), and this improvement is found to increase the $4f^{13}$–$4f^{13}5d(t_{2g})^1$ energy differences by some 25000 cm^{-1} in average, as it can be seen in Table I. The large transition energy corrections due to dynamic electron correlation can be associated with the fact that electron correlation is much larger for tight $4f$–$4f$ electron pairs than for far more separated $4f$–$5d$ electron pairs and the number of $4f$–$4f$ pairs substituted by $4f$–$5d$ pairs in the $4f^N$–$4f^{N-1}5d^1$ interconfigurational transitions is largest for N=14.

If we concentrate now on the best spin-orbit free results, the following conclusions, relative to the high-spin and low-spin $4f^{13}5d(t_{2g})^1$ states and their energy differences, can be drawn (see MS-CASPT2 results in Table I and potential energy surfaces on the left of Figure 1). (i) The lowest high-spin state, 1^3T_{1u}, appears to be well separated in energy from the rest of $^{3,1}\Gamma$ terms of the manifold by an energy gap of about 2700 cm^{-1}. (ii) The remaining high- and low-spin states are significantly closer to each other in energy. This is particularly so for the three $^1T_{1u}$ states of the $4f^{13}5d(t_{2g})^1$ manifold (see dashed curves on the left of Figure 1). The latter is relevant because, in the absence of spin-orbit coupling, the $1^1A_{1g} \rightarrow i^1T_{1u}$ transitions are the only electric dipole allowed transitions, and hence, it is the $^1T_{1u}$ character of the spin-orbit excited states what enables electric dipole allowed transitions.

B. Spin-orbit coupling results: High-spin and low-spin character of the $4f^{13}\mathbf{5}d(t_{2g})^1$ states and spectral features

Once scalar relativistic effects and dynamic electron correlation have been accounted for, it is possible to proceed to the second step to include spin-orbit coupling as well. We discuss

here the results of the spin-orbit CI calculations described in Section II for the $4f^{13}5d(t_{2g})^1$ manifold; they appear in Table II and on the right of Figure 1. We have also calculated the $4f^{14}$–$4f^{13}5d(t_{2g})^1$ absorption spectrum using the results of Table II; it is shown in Fig. 2 (see Section II for details).

The importance of spin-orbit coupling in this Yb containing material becomes evident if the calculated potential energy surfaces of the $4f^{13}5d(t_{2g})^1$ manifold in Figure 1 are compared. A major effect is the splitting of the manifold into two submanifolds which, using free ion language, correspond to the splitting of the $4f^{13}$ subshell into $4f^{13}[J{=}7/2]$ and $4f^{13}[J{=}5/2]$ components. Consequently with this, the $4f^{14}{\rightarrow}4f^{13}5d(t_{2g})^1$ absorption spectrum shows an energy gap of some 6000 cm^{-1} between the bands associated with excitations to $6T_{1u}$ and $7T_{1u}$, as indicated in Fig. 2. This effect becomes visible in this lanthanide system because the spin-orbit effects on the $4f^{13}$ subshell are dominant, whereas the crystal field effects on the $4f^{13}$ subshell (resulting here from the interactions with the Br ligands in the cluster and the interactions with the $CsCaBr_3$ AIMP embedding) are relatively small. This type of splitting is not observed in similar actinide systems, like U^{4+} containing crystals, where the spin-orbit and crystal effects on the $5f^1$ subshell are of comparable magnitude and the $5f^16d(t_{2g})^1$ manifold is not split into equivalent $5f^1[5/2]6d(t_{2g})^1$ and $5f^1[7/2]6d(t_{2g})^1$ submanifolds.[42]

We can discuss now the high- and low-spin character of the $4f^{13}5d(t_{2g})^1$ states and how it affects the spectral features taking into account the composition of the spin-orbit wave functions presented in Table II. The lowest states of the $4f^{13}[7/2]5d(t_{2g})^1$ submanifold are most relevant, since they should be responsible for the first absorption/emission bands.

First of all, we can observe the consequences of the energy separation of the lowest high-spin state 1^3T_{1u} in the spin-orbit results (Fig. 1 right and Table II): States $1T_{2u}(90\%1^3T_{1u})$ and $1E_u(90\%1^3T_{1u})$ can be clearly identified as two of its spin-orbit components, given their dominant 1^3T_{1u} character; furthermore, they are also separated in energy from the next higher state by 2600 cm^{-1}. These states give electric dipole forbidden $A_{1g}{\rightarrow}1T_{2u}$,$1E_u$ absorptions and lead to a first, relatively low intensity vibronic absorption band which we indicate as a vertical bar in Fig. 2.

In contrast, the proximity of the remaining terms, commented in the previous Subsection (Fig. 1, left), results in significant spin-orbit mixing, which is apparent in the next higher spin-orbit states (Table II), $2E_u$ (41% 2^1E_u, 37% 2^3T_{2u}), $1T_{1u}$ (38% 2^3T_{1u}, 34% 1^1T_{1u}), $2T_{1u}$

(32% 1^3T_{1u}, 15% 2^1T_{1u}), and also in most spin-orbit states. As a result of this mixing none of the spin-orbit states calculated shows dominant spin singlet character. In particular, the three $^1T_{1u}$ enabling states mix so strongly with other terms that the total $^1T_{1u}$ character of the electric dipole allowed T_{1u} states is always smaller than 45%, and it can be observed that the total $^1T_{1u}$ character of the three more intense bands in the calculated spectrum, which are associated with origins $2T_{1u}$, $7T_{1u}$, and $8T_{1u}$, is 32, 30, and 42%, respectively.

As we have just discussed, this very different electronic structure is related to the fact that the 1^3T_{1u} state is isolated from the rest of close-lying terms by an energy gap $E_{gap}(1^3T_{1u}) = 2700$ cm^{-1}, and it is separated from the first enabling low-spin state, 1^1T_{1u}, by $\Delta E(1^3T_{1u} \rightarrow 1^1T_{1u}) = 3900$ cm^{-1}. In order to show this, we have conducted the following computational experiments: We have calculated the vertical $4f^{14} \rightarrow 4f^{13}5d(t_{2g})^1$ transition energies at the SO-CI level of calculation shifting the energy of the high-spin 1^3T_{1u} state by $E_{shift}(1^3T_{1u}) = +2700$, +1350, 0, and -2700 cm^{-1} in the $sfss$ spin-orbit Hamiltonian, so that the energy gap above 1^3T_{1u} is 0, 1400, 2700, and 5400 cm^{-1}, respectively, and the energy difference between the high- and low-spin states $\Delta E(1^3T_{1u} \rightarrow 1^1T_{1u})$ varies from 1200 to 2600, 3900, and 6600 cm^{-1}, respectively. (A selection of the results of these numerical experiments appears in Fig. 3 and Table III; they correspond to a fixed Yb–Br distance, R(Yb–Br)=2.707 Å.) In effect, it can be observed that, as the energy gap above 1^3T_{1u} increases from 0 to 5400 cm^{-1}, the energy separation between the first forbidden band, due to $1T_{2u}$ and $1E_u$ and the first allowed band, associated with $1T_{1u}$ and $2T_{1u}$, increases (see Table III and Fig. 3). At the same time, $1T_{2u}$ and $1E_u$ show increasingly pure 1^3T_{1u} character (see Table III). Furthermore, the energy difference between the forbidden and allowed bands, increases with slope close to 1 up to $E_{gap}(1^3T_{1u})$=2700 cm^{-1} (Fig. 3), where an avoided crossing between $1T_{1u}$ and $2T_{1u}$ occurs, which corresponds to a significant change in their electronic structure (cf. the composition of their wave functions in Table III), so that, as the largest energy gap used is approached, the composition of the $1T_{1u}$ wave function reveals that this state is becoming the T_{1u} component of 1^3T_{1u}, this indicating an evolution towards a pure Landé type of splitting corresponding to an isolated 1^3T_{1u}, whose four octahedral double group components are $1T_{2u}$, $1E_u$, $1T_{1u}$, and $3A_{1u}$.

Altogether, the whole absorption spectrum of Fig. 2 shows a first low intensity band on the low energy side of the spectrum followed by several strong absorption bands, in agreement with previous observations in heavy Ln^{3+} and Ln^{2+} ions, as discussed in the

Introduction. The electronic structure of the states leading to these two types of excitations is very different, as we have just discussed. Whereas the forbidden band can be described as "spin-forbidden" transitions involving "high-spin" excited states, the next allowed band and all other allowed bands in Fig. 2, cannot be described as "spin-allowed" transitions involving "low-spin" excited states as usually accepted. Rather, they can be described as "spin-enabled" transitions involving excited states with strong spin-orbit mixing which can neither be labeled as high-spin states nor as low-spin states, and which get their intensity from limited (smaller than 45%) enabling $^1T_{1u}$ character.

The only experimental report on Yb^{2+}-doped $CsCaBr_3$ crystals is that of Ref. 10, as far as we know. The emission spectrum at 77 K was presented showing two broad, structureless bands separated by some 1640 cm^{-1}. The lowest band is significantly less intense than the second band at 77K and their peak positions can be roughly estimated to lie around 23000 and 24500 cm^{-1}. According to our results the lower band should correspond to vibronic emissions from $1T_{2u}$ and $1E_u$ (both origins are calculated at 23900 cm^{-1}) whereas the higher band should correspond to a superposition of vibronic emission from $2E_u$ and electric dipole allowed emissions from $1T_{1u}$ and $2T_{1u}$ in thermal equilibrium (these origins are found at 25500–25600 cm^{-1}). The experimental spectrum at 300 K shows the higher band loses intensity in favor of the lower one, which can be interpreted in terms of multiphonon relaxation being favored at room temperature.[3,7]

IV. CONCLUSIONS

We have calculated the $4f^{14} \rightarrow 4f^{13}5d(t_{2g})^1$ absorption spectrum of $CsCaBr_3$:Yb^{2+} crystals using wave function based relativistic methods of quantum chemistry. It is made of a first low intensity band on the low energy side followed by several strong absorption bands. The electronic structure of the states leading to these two types of excitations appears to be very different and the following conclusions can be drawn relative to their high-spin and low-spin character: (1) The forbidden band can be described as due to "spin-forbidden" transitions involving "high-spin" excited states because their 1^3T_{1u} character is 90%. (2) The allowed bands cannot be described as "spin-allowed" transitions involving "low-spin" excited states; they can neither be described as orbitally allowed transitions to predominantly high-spin states, because the excited states involved are an extensive mixture of terms of

different spin and spatial symmetries. (3) The allowed bands can be described as "spin-enabled" transitions because they get their intensity from their limited (smaller than 45%) $^1T_{1u}$ enabling character.

As revealed by a numerical experiment with a spin-orbit free Hamiltonian, this very different electronic structure is related to the fact that the $4f^{13}5d(t_{2g})^1$ manifold is split by an energy gap which separates the lowest 1^3T_{1u} from the rest of terms, which, in turn, lie very close in energy from each other. As a consequence, the lowest spin-orbit components of 1^3T_{1u} remain 90% pure, whereas strong spin-orbit coupling is observed between the remaining $4f^{13}5d(t_{2g})^1$ terms, among which the 1–3 $^1T_{1u}$ enabling ones lie. As a result there is a widespread electric dipole enabling $^1T_{1u}$ character, which, although never higher than 45%, leads to a number of spin-enabled absorption bands.

Acknowledgments

This research was supported in part by Ministerio de Ciencia e Innovación, Spain, under contracts CTQ2005-08550 and MAT2008-05379. G.S-S. acknowledges an FPI fellowship from Ministerio de Ciencia e Innovación, Spain.

---

* Corresponding author; Electronic address: `zoila.barandiaran@uam.es`

[1] L. van Pieterson, M. F. Reid, R. T. Wegh, S. Soverna, and A. Meijerink, Phys. Rev. B **65**, 045113 (2002).

[2] L. van Pieterson, M. F. Reid, G. W. Burdick and A. Meijerink, Phys. Rev. B **65**, 045114 (2002).

[3] Z. Pan, C. Duan, and P. A. Tanner, Phys. Rev. B **77**, 085114 (2008).

[4] C. K. Jørgensen and J. S. Brinen, Mol. Phys. **6**, 629 (1963).

[5] R. T. Wegh and A. Meijerink, Phys. Rev. B **60**, 10820 (1999).

[6] L. van Pieterson, R. T. Wegh, A. Meijerink, and M. F. Reid, J. Chem. Phys. **115**, 9382 (20010).

[7] J. Grimm and H. U. Güdel, Chem. Phys. Lett. **404**, 40 (2005).

[8] J. Grimm, E. Beurer, and H. U. Güdel, Inorg. Chem. **45**, 10905 (2006).

[9] E. Beurer, J. Grimm, P. Gerner and H. U. Güdel, J. Amer. Chem. Soc. **128**, 3110 (2006).

[10] P. Larsen, M. Adlung, and C. Wickleder, Rare Earth Conference, Wroclaw, 2006 (unpublished), Abstract CI3.

[11] J. Grimm, O. S. Wenger, K. W. Krämer and H. U. Güdel, J. Lumin. **126**, 590 (2007).

[12] G. Sánchez-Sanz, L. Seijo, and Z. Barandiarán. To be published.

[13] P. A. Tanner, C. S. K. Mak, N. M. Edelstein, K. M. Murdoch, G. Liu, J. Huang, L. Seijo, , and Z. Barandiarán, J. Amer. Chem. Soc. **125**, 13225 (2003).

[14] J. Gracia, L. Seijo, Z. Barandiarán, D. Curulla, H. Niemansverdriet, and W. van Gennip, J. Lumin. **128**, 1248 (2008).

[15] B. Ordejón, L. Seijo, and Z. Barandiarán, J. Chem. Phys. **126**, 194712 (2007).

[16] F. Ruipérez, Z. Barandiarán, and L. Seijo, J. Chem. Phys. **127**, 144712 (2007).

[17] Z. Barandiarán and L. Seijo, J. Chem. Phys. **89**, 5739 (1988).

[18] L. Seijo and Z. Barandiarán, in *Computational Chemistry: Reviews of Current Trends*, edited by J. Leszczyński (World Scientific, Singapore, 1999), vol. 4, p. 55.

[19] B. O. Roos, P. R. Taylor, and P. E. M. Siegbahn, Chem. Phys. **48**, 157 (1980); P. E. M. Siegbahn, A. Heiberg, J. Almlöf, and B. O. Roos, J. Chem. Phys. **74**, 2384 (1981); P. Siegbahn, A. Heiberg, B. Roos, and B. Levy, Phys. Scr. **21**, 323 (1980).

[20] K. Andersson, P.-Å. Malmqvist, B. O. Roos, A. J. Sadlej, and K. Wolinski, J. Phys. Chem. **94**, 5483 (1990).

[21] K. Andersson, P.-Å. Malmqvist and B. O. Roos, J. Chem. Phys. **96**, 1218 (1992).

[22] J. Finley, P.-Å. Malmqvist, B. O. Roos and L. Serrano-Andrés, Chem. Phys. Lett. **288**, 299 (1998).

[23] A. Zaitsevskii and J. P. Malrieu, Chem. Phys. Lett. **233**, 597 (1995).

[24] H. J. Seifert and D. Haberhauer, Z. Anorg. Allg. Chem. **491**, 301 (1982).

[25] H. M. Evjen, Phys. Rev. **39**, 675 (1932).

[26] L. Seijo, Z. Barandiarán, and B. Ordejón, Mol. Phys. **101**, 73 (2003).

[27] Z. Barandiarán and L. Seijo, Can. J. Chem. **70**, 409 (1992).

[28] L. Seijo, Z. Barandiarán, and E. Harguindey, J. Chem. Phys. **114**, 118 (2001).

[29] J. Andzelm, M. Klobukowski, E. Radzio-Andzelm, Y. Sakai, and H. Tatewaki, *Gaussian Basis Sets for Molecular Calculations*, edited by S. Huzinaga, (Elsevier, Amsterdam, 1984).

[30] From B. Roos unpublished ANO-RCC basis set for Br included in the MOLCAS basis set libraries.

[31] L. Seijo, J. Chem. Phys. **102**, 8078 (1995).

[32] L. Seijo and Z. Barandiarán, J. Chem. Phys. **118**, 5335 (2003).

[33] G. Karlström, R. Lindh, P. A. Malmqvist, B. O. Roos, U. Ryde, V. Veryazov, P. O. Widmark, M. Cossi, B. Schimmelpfennig, P. Neogrady, and L. Seijo, Comput. Mater. Sci. **28**, 22 (2003).

[34] Z. Barandiarán and L. Seijo, J. Chem. Phys. **118**, 7439 (2003).

[35] R. Llusar, M. Casarrubios, Z. Barandiarán, and L. Seijo, J. Chem. Phys. **105**, 5321 (1996).

[36] COLUMBUS suite of programs. (ARGOS, CNVRT, SCFPQ, LSTRN, CGDBG, and CIDBG.) R. M. Pitzer (principal author). See: A. H. H. Chang and R. M. Pitzer, J. Am. Chem. Soc. **111**, 2500 (1989), and references therein for a description. CNVRT and LSTRN have been adapted to handle AIMP integrals by L. Seijo. CIDBG has been modified for spin-free-state-shifted spin-orbit CI calculations by M. Casarrubios.

[37] V. Vallet, L. Maron, C. Teichteil, and J.-P. Flament , J. Chem. Phys. **113**, 1391 (2000).

[38] Detailed core and embedding AIMP data libraries in electronic format are available from the authors upon request or directly at the address http://www.uam.es/quimica/aimp/Data/-AIMPLibs.html. See also Ref. 33.

[39] E. J. Heller, J. Chem. Phys. **62**, 1544 (1975).

[40] E. J. Heller, Acc. Chem. Res. **14**, 368 (1981).

[41] J. I. Zink and K. S. Shin, *Molecular distortions in excited electronic states determined from electronic and resonance raman spectroscopy* (Wiley, New York, 1991), vol. 16 of *Advances in Photochemistry*, pp. 119–214.

[42] B. Ordejón, M. Karbowiak, L. Seijo and Z. Barandiarán, J. Chem. Phys. **125**, 074511 (2006).

TABLE I: Spectroscopic constants of the $4f^{13}5d(t_{2g})^1$ states of the $(YbBr_6)^{4-}$ cluster embedded in $CsCaBr_3$. Spin-free Hamiltonian calculations. Yb–Br bond distances, R_e, in Å; totally symmetric vibrational frequencies, $\bar{\nu}_{a_{1g}}$, in cm^{-1}; and minimum-to-minimum energy differences, T_e, relative to the $4f^{14}$–1^1A_{1g} ground state, in cm^{-1}. Manifold averages and mean square deviations of the individual values with respect to the averages are labeled as $\langle 4f^{13}5d(t_{2g})^1\rangle$.

	CASSCF($4f$,$5d$,$6s$)			MS-CASPT2(Br48,Yb32)		
state	R_e	$\bar{\nu}_{a_{1g}}$	T_e	R_e	$\bar{\nu}_{a_{1g}}$	T_e
$1\ ^1A_{1g}$	2.820	192	0	2.732	184	0
$\langle 4f^{13}5d(t_{2g})^1\rangle$	2.796±0.001	192±1		2.703±0.002	187±1	
$1\ ^3T_{1u}$	2.799	193	2302	2.708	185	28406
$2\ ^3T_{1u}$	2.797	192	5637	2.705	188	31098
$1\ ^3E_u$	2.797	192	5401	2.705	188	31469
$1\ ^3T_{2u}$	2.797	192	5582	2.704	188	31685
$1\ ^1E_u$	2.796	192	6404	2.705	189	32039
$1\ ^1T_{2u}$	2.796	193	6655	2.701	188	32194
$1\ ^1T_{1u}$	2.797	193	7285	2.701	184	32328
$1\ ^3A_{2u}$	2.795	192	7717	2.704	186	32397
$2\ ^1T_{1u}$	2.797	192	8969	2.700	188	33281
$2\ ^3T_{2u}$	2.795	192	8281	2.703	188	33286
$2\ ^1E_u$	2.795	191	8368	2.703	188	33365
$3\ ^3T_{1u}$	2.796	192	9057	2.703	187	33382
$2\ ^3E_u$	2.795	191	8239	2.704	188	33653
$1\ ^1A_{1u}$	2.794	192	9722	2.704	188	34285
$3\ ^1T_{1u}$	2.797	192	11531	2.700	186	34362
$1\ ^3A_{1u}$	2.794	192	9754	2.703	188	34505
$1\ ^1A_{2u}$	2.793	191	10238	2.703	187	34886
$2\ ^1T_{2u}$	2.795	192	9910	2.703	187	34901

TABLE II: Results of the calculations on the $(YbBr_6)^{4-}$ cluster that include $CsCaBr_3$ embedding, 80 valence electron correlation, and relativistic effects, including spin-orbit coupling. Yb–Br bond distances, R_e, in Å; totally symmetric vibrational frequencies, $\bar{\nu}_{a_{1g}}$, in cm^{-1}; minimum-to-minimum energy differences, T_e, relative to the $4f^{14}$–$1A_{1g}$ ground state, in cm^{-1}; absorption oscillator strengths, f; and analyses of the spin-orbit wave functions. Manifold averages and mean square deviations of the individual values with respect to the averages are labeled as $\langle 4f^{13}5d(t_{2g})^1\rangle$.

state	R_e	$\bar{\nu}_{a_{1g}}$	T_e	$f \times 10^2$ [1]	Weights of spin-orbit free wave functions [2]					
1 A_{1g}	2.732	185	0							
$\langle 4f^{13}5d(t_{2g})^1\rangle$	2.704±0.001	186±2								
				$4f^{13}[7/2(^2F)]\times 5d(t_{2g})^1$ submanifold						
1 T_{2u}	2.708	186	23890		89.98	01 $^3T_{1u}$				
1 E_u	2.708	186	23902		90.02	01 $^3T_{1u}$	5.64	01 $^3T_{2u}$		
2 E_u	2.706	188	26544		41.25	01 ^1E_u	36.64	02 $^3T_{1u}$	16.13	01 $^3T_{2u}$
1 T_{1u}	2.705	184	26555	0.273	37.59	02 $^3T_{1u}$	33.99	01 $^1T_{1u}$	11.74	01 ^3E_u
					9.49	01 $^3T_{1u}$				
2 T_{1u}	2.705	184	26598	1.260	32.20	01 $^3T_{1u}$	15.20	02 $^1T_{1u}$	13.59	01 $^3T_{2u}$
					11.76	02 $^3T_{1u}$	10.49	03 $^1T_{1u}$	6.57	01 $^1T_{1u}$
					5.66	03 $^3T_{1u}$				
2 T_{2u}	2.704	189	26718		33.91	01 $^1T_{2u}$	32.40	01 ^3E_u	21.50	02 $^3T_{1u}$
					9.54	01 $^3T_{2u}$				
1 A_{1u}	2.705	186	27132		94.34	02 $^3T_{1u}$				
3 T_{2u}	2.704	188	27160		63.10	01 $^3T_{2u}$	11.98	01 ^3E_u	9.72	02 $^3T_{1u}$
					5.43	03 $^3T_{1u}$				
3 T_{1u}	2.705	187	27200	0.030	45.13	01 ^3E_u	24.15	02 $^3T_{1u}$	11.99	01 $^3T_{2u}$
					9.17	02 $^3T_{2u}$				
1 A_{2u}	2.704	188	27292		93.26	01 $^3T_{2u}$				
4 T_{2u}	2.704	186	28008		43.81	02 $^3T_{2u}$	41.93	01 $^3A_{2u}$	5.20	02 ^3E_u
3 E_u	2.704	187	28264		54.82	03 $^3T_{1u}$	27.55	02 ^1E_u	13.73	01 $^3T_{2u}$
4 T_{1u}	2.704	186	28355	0.000	47.20	02 ^3E_u	31.81	02 $^3T_{2u}$	9.42	01 $^1T_{1u}$
5 T_{1u}	2.703	183	29072	0.084	28.23	02 $^1T_{1u}$	21.17	02 $^3T_{2u}$	15.98	03 $^1T_{1u}$
					12.30	01 $^3T_{2u}$	8.18	01 $^3A_{1u}$	5.66	01 $^3T_{1u}$
4 E_u	2.704	187	29107		56.64	02 $^3T_{2u}$	19.17	02 ^1E_u	14.08	01 ^1E_u
					5.23	03 $^3T_{1u}$				

5 T_{2u}	2.703	187	29209		54.29	03 $^3T_{1u}$	17.94	02 ^3E_u	12.43	01 $^1T_{2u}$
					5.48	02 $^1T_{2u}$	5.46	01 ^3E_u		
2 A_{1u}	2.704	186	29231		48.89	01 $^1A_{1u}$	42.10	03 $^3T_{1u}$		
6 T_{2u}	2.703	187	29655		39.70	02 $^1T_{2u}$	26.06	02 ^3E_u	15.77	01 $^3A_{2u}$
					5.78	01 ^3E_u				
6 T_{1u}	2.703	186	29884	0.489	43.21	03 $^3T_{1u}$	38.70	01 $^3A_{1u}$		
2 A_{2u}	2.703	187	29992		47.59	02 $^3T_{2u}$	45.80	01 $^1A_{2u}$	6.46	01 $^3T_{2u}$
$4f^{13}[5/2(^2F)]\times5d(t_{2g})^1$ submanifold										
3 A_{1u}	2.707	186	34560		93.95	01 $^3T_{1u}$				
7 T_{1u}	2.707	182	35916	1.524	40.38	01 $^3T_{1u}$	29.72	03 $^1T_{1u}$	15.27	01 $^3T_{2u}$
					8.84	01 ^3E_u				
7 T_{2u}	2.706	186	36508		54.03	02 $^3T_{1u}$	32.35	01 ^3E_u	6.41	02 ^3E_u
5 E_u	2.705	187	36725		41.87	01 $^3T_{2u}$	37.28	02 $^3T_{1u}$	12.65	02 ^1E_u
6 E_u	2.705	188	37334		40.14	01 ^1E_u	25.92	02 $^3T_{2u}$	14.54	02 $^3T_{1u}$
					10.89	01 $^3T_{2u}$				
8 T_{2u}	2.703	189	37420		42.27	01 $^1T_{2u}$	16.65	01 $^3T_{2u}$	8.89	03 $^3T_{1u}$
					6.78	01 ^3E_u	6.44	01 $^3A_{2u}$	5.56	01 $^3T_{1u}$
8 T_{1u}	2.706	182	37503	2.304	32.16	01 $^3T_{2u}$	21.80	02 $^1T_{1u}$	19.72	03 $^1T_{1u}$
					15.48	01 ^3E_u				
9 T_{1u}	2.703	184	38301	0.033	37.78	01 $^1T_{1u}$	15.61	02 $^3T_{1u}$	12.29	01 $^3T_{2u}$
					11.15	01 ^3E_u	10.78	02 ^3E_u		
9 T_{2u}	2.704	186	39146		34.52	02 ^3E_u	29.82	02 $^3T_{2u}$	16.87	03 $^3T_{1u}$
					7.44	02 $^1T_{2u}$	6.10	01 $^3A_{2u}$		
3 A_{2u}	2.703	186	39319		51.16	01 $^1A_{2u}$	48.40	02 $^3T_{2u}$		
7 E_u	2.704	186	39350		33.82	03 $^3T_{1u}$	32.88	02 ^1E_u	12.65	02 $^3T_{2u}$
					11.30	01 $^3T_{2u}$	5.49	02 $^3T_{1u}$		
10 T_{2u}	2.703	186	39459		39.77	02 $^1T_{2u}$	24.27	01 $^3A_{2u}$	16.19	02 $^3T_{2u}$
					9.23	03 $^3T_{1u}$				
10 T_{1u}	2.703	186	39518	0.165	32.78	03 $^3T_{1u}$	22.81	02 $^3T_{2u}$	17.46	02 ^3E_u
					14.99	01 $^3A_{1u}$				
4 A_{1u}	2.704	186	39716		55.25	03 $^3T_{1u}$	42.76	01 $^1A_{1u}$		
11 T_{1u}	2.703	184	39830	0.021	28.49	01 $^3A_{1u}$	20.20	02 $^1T_{1u}$	18.06	02 ^3E_u
					10.38	02 $^3T_{2u}$	9.25	03 $^1T_{1u}$	8.10	03 $^3T_{1u}$

[1] Oscillator strenghs for the $1A_{1g} \rightarrow iT_{1u}$ absorptions were calculated at the ground state equilibrium distance: 2.732 Å

[2] Weights (in %) larger than 5% are given. They have been calculated at R(Yb-Br)=2.705 Å.

TABLE III: Results of spin-orbit CI calculations where the energy of 1^3T_{1u} is shifted relative to its actual value in the $sfss$ spin-orbit Hamiltonian an amount $E_{shift}(1^3T_{1u})$. Energy gap above 1^3T_{1u}, $E_{gap}(1^3T_{1u})$, and vertical transition energies are given in cm^{-1}. Weights of spin-orbit free wave functions are given in % if larger than 10%.

$E_{shift}(1^3T_{1u})$		+2700	+1400	0	–2700
$E_{gap}(1^3T_{1u})$		0	1400	2700	5400
$\Delta E(1^3T_{1u} \rightarrow 1^1T_{1u})$		1200	2600	3900	6600
$\Delta E(1T_{2u} \rightarrow 1E_u)$		56	54	54	52
$\Delta E(1T_{2u} \rightarrow 1T_{1u})$		399	1560	2700	3798
$\Delta E(1T_{2u} \rightarrow 2T_{1u})$		891	1991	2762	5192
$\Delta E(1T_{2u} \rightarrow 3A_{1u})$		10862	10718	10646	10669
State		Weights of spin-orbit free wave functions			
$1T_{2u}$	1^3T_{1u}	74	87	90	93
$1E_u$	1^3T_{1u}	73	87	90	93
$1T_{1u}$	1^3T_{1u}				62
	2^3T_{1u}	49	49	38	
	1^1T_{1u}	41	41	34	
$2T_{1u}$	1^3E_u	54	42		
	1^3T_{1u}		13	32	
	2^3T_{1u}	21	12	12	49
	1^1T_{1u}				41
	2^1T_{1u}		15	15	
$3A_{1u}$	1^3T_{1u}	92	94	94	85

FIG. 1: Breathing mode potential energy curves of the $4f^{13}5d(t_{2g})^1$ manifold of $CsCaBr_3$:$(YbBr_6)^{4-}$. All results include embedding effects and electron correlation. Left: spin-orbit free MS-CASPT2(Br48,Yb32) calculations; $^1T_{1u}$ states are plotted with dashed lines. Right: spin-orbit CI calculations. T_{1u} states are plotted with dashed lines. The symmetries of the lowest two states of the two differentiated $4f^{13}(7/2)5d(t_{2g})^1$ and $4f^{13}(5/2)5d(t_{2g})^1$ manifolds are indicated. See text for details.

FIG. 2: Calculated absorption spectrum of $CsCaBr_3$:$(YbBr_6)^{4-}$ using spin-orbit CI data from Table II and different values for the line broadening parameter (40 and 5 cm^{-1} in the low and high resolution spectra, respectively). Electronic origins iT_{1u} are indicated for i = 1, 2, 5, 6, 7, 8, 10. The first two electric dipole forbidden electronic origins ($1A_{1g}$→$1T_{2u}$, $1E_u$) are indicated as vertical bars.

FIG. 3: Variation of vertical energy differences (relative to $1T_{2u}$) with the energy gap above 1^3T_{1u} and with the energy difference between high- and low-spin states $\Delta E(1^3T_{1u}\rightarrow 1^1T_{1u})$. Only the lowest states of the $4f^{13}[7/2]5d(t_{2g})^1$ and $4f^{13}[5/2]5d(t_{2g})^1$ submanifolds are presented. Calculations correspond to fixed Yb–Br distance, R(Yb–Br)=2.707 Å.

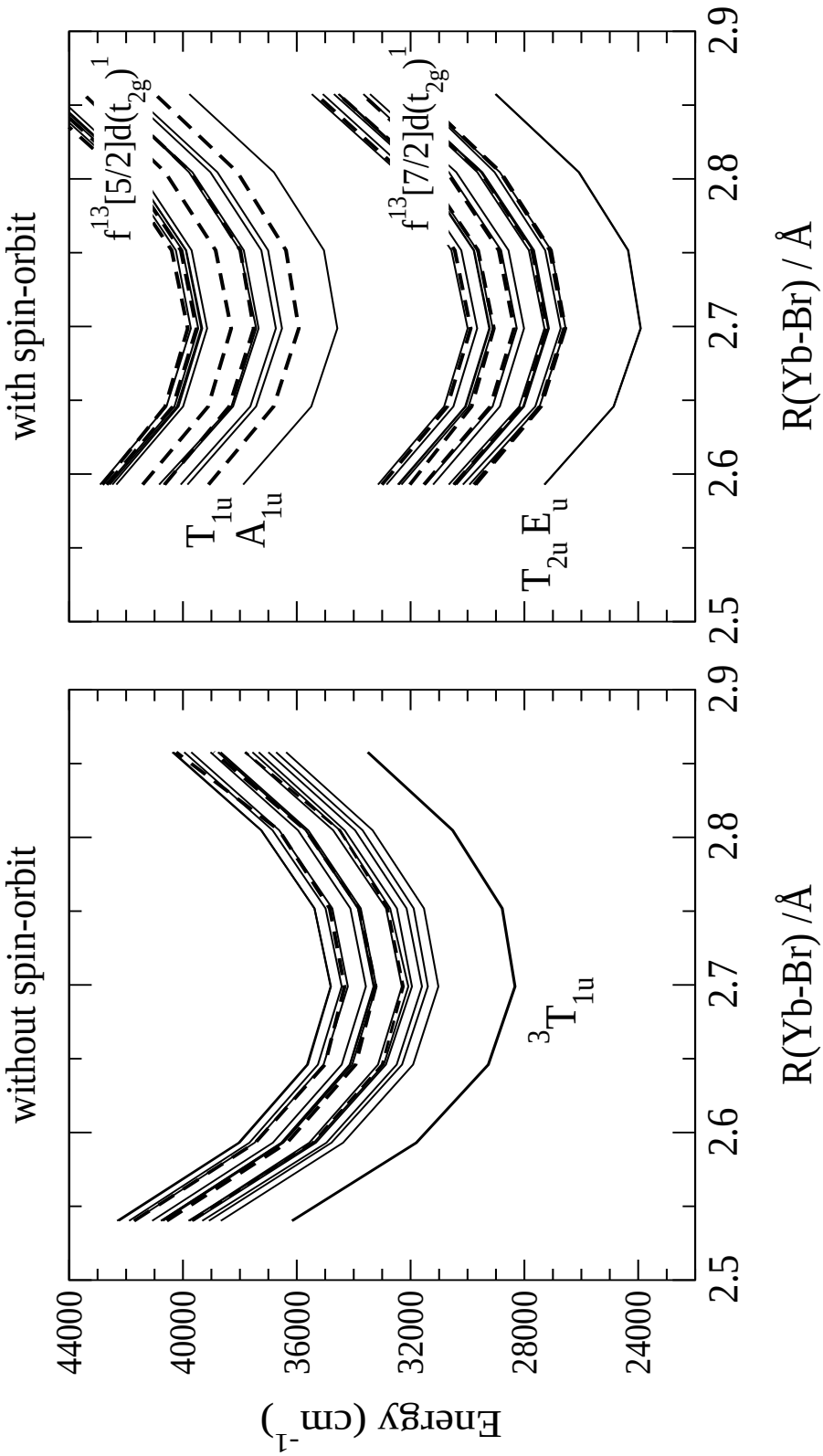

Figure 1. Sánchez-Sanz *et al.*, The Journal of Chemical Physics

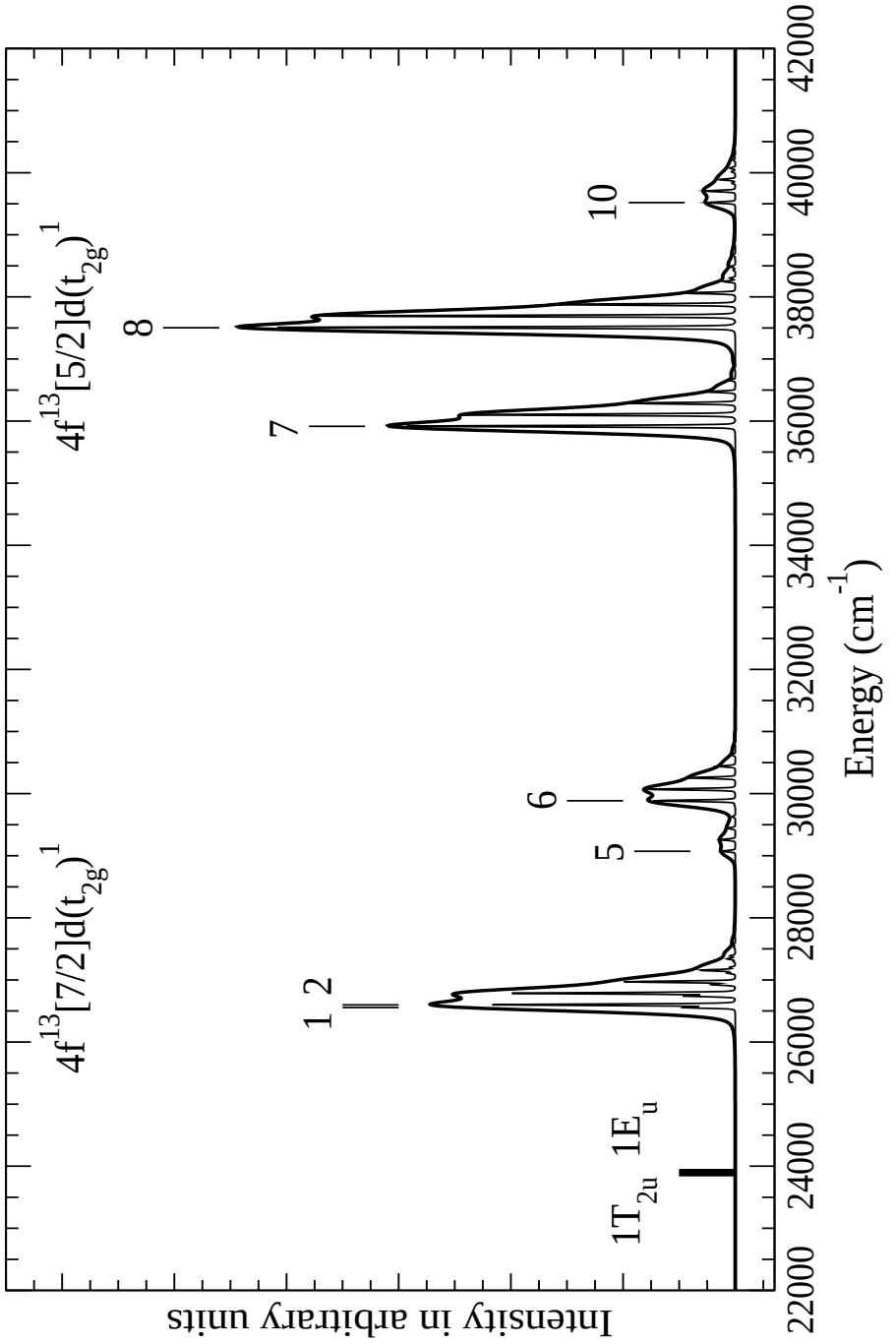

Figure 2. Sánchez-Sanz *et al.*, The Journal of Chemical Physics

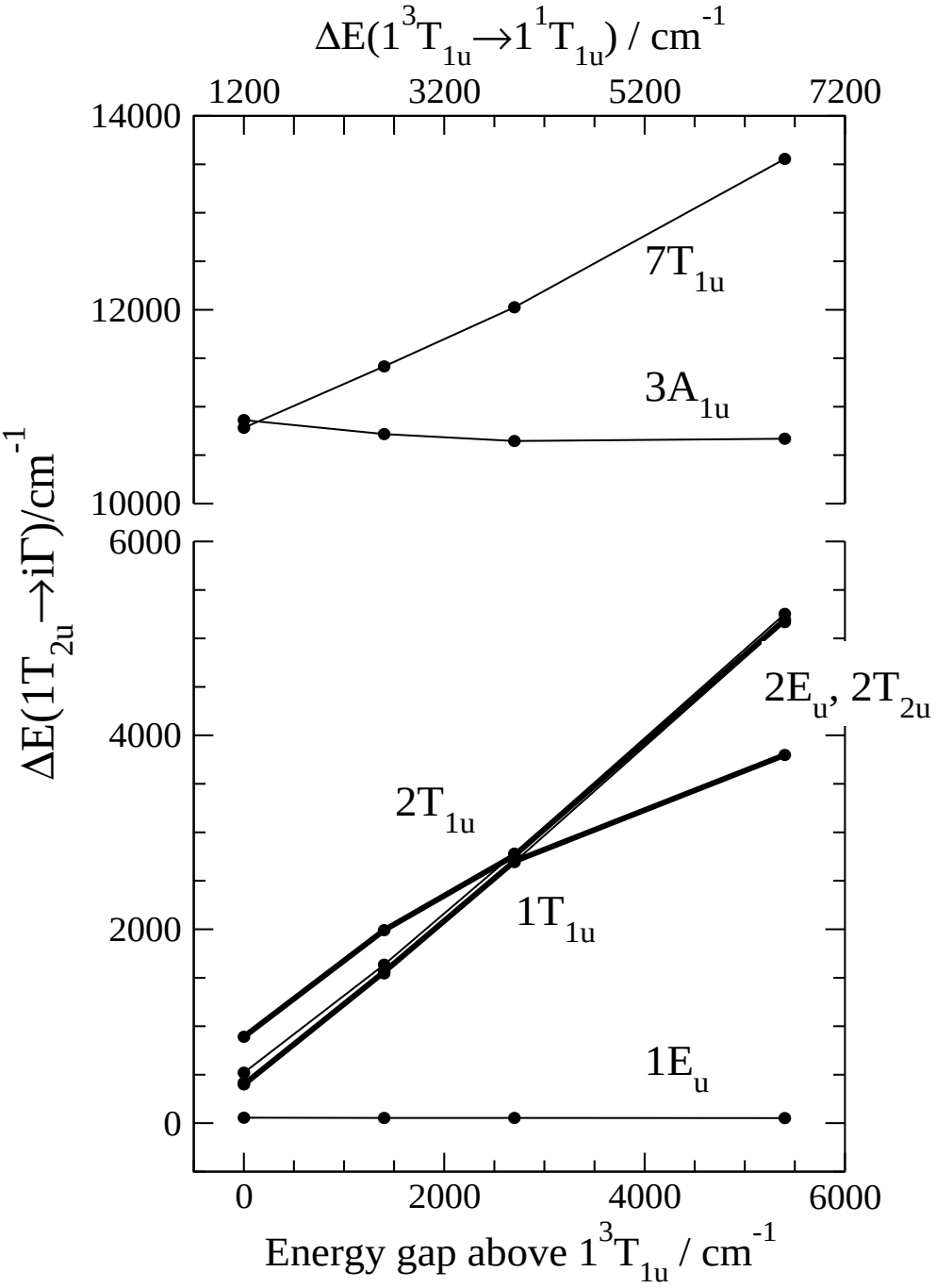

Figure 3. Sánchez-Sanz *et al.*, The Journal of Chemical Physics